Bio-Design and Manufacturing (2026) 9:379–398
https://doi.org/10.1631/bdm.2500337

RESEARCH ARTICLE

Novel bromoacetophenone-accelerated visible-light 3D and 4D printing methods for rapid fabrication of biocompatible and structurally dynamic scaffolds

Nima Tabatabaei Rezaei[1] · Kartikeya Dixit[1] · Ashna Rajeev[2] · Karla Villegas[3] · Giovanniantonio Natale[4] · Frederic Menard[5] · Hitendra Kumar[6] · Keekyoung Kim[1,7]

Received: 3 July 2025 / Accepted: 28 September 2025 / Published online: 16 March 2026

Abstract

Rapid and accurate visible-light photopolymerization is essential for advancing bioprinted engineered tissues. In this study, we developed a novel three-component photoinitiator system for visible light-induced crosslinking of gelatin methacryloyl (GelMA) hydrogels, designed to improve polymerization kinetics, mechanical strength, and structural integrity. Incorporation of 2-bromoacetophenone (BAP) considerably accelerated photopolymerization, with reaction rates increasing alongside BAP concentration, enabling the rapid fabrication of stable hydrogel scaffolds. Printing experiments confirmed that BAP promoted fast crosslinking of GelMA bioinks under visible light, reducing printing time while preserving high-resolution structural features. Additionally, the incorporation of BAP induced microscale structural transformations in the hydrogels during hydration, as evidenced by scanning electron microscopy imaging and swelling analyses. This unique property enabled the fabrication of multilayer constructs exhibiting time-dependent deformation, demonstrating four-dimensional (4D) printing capabilities. Moreover, biocompatibility evaluations revealed that cells maintained high viability in BAP-containing hydrogels. Overall, the BAP-based photoinitiator system offers a promising strategy for high-speed, high-resolution bioprinting, combining enhanced mechanical performance, reduced fabrication time, and dynamic structural adaptability—features that make it highly suitable for advanced biofabrication and tissue engineering applications.

✉ Hitendra Kumar
hitendra@iiti.ac.in

✉ Keekyoung Kim
keekyoung.kim@ucalgary.ca

[1] Department of Mechanical and Manufacturing Engineering, University of Calgary, Calgary, Alberta T2N 1N4, Canada

[2] Department of Chemical Engineering, University of Waterloo, Waterloo, Ontario N2L 3G1, Canada

[3] School of Engineering and Sciences, Tecnológico de Monterrey, Zapopan, Jalisco 45201, Mexico

[4] Department of Chemical & Petroleum Engineering, Schulich School of Engineering, University of Calgary, Calgary, AB T2N 1N4, Canada

[5] Department of Chemistry, The University of British Columbia, Kelowna, British Columbia V1V 1V7, Canada

[6] Department of Biosciences and Biomedical Engineering, Indian Institute of Technology Indore, Indore, Madhya Pradesh 453552, India

[7] Department of Biomedical Engineering, University of Calgary, Calgary, Alberta T2N 1N4, Canada

Graphical abstract

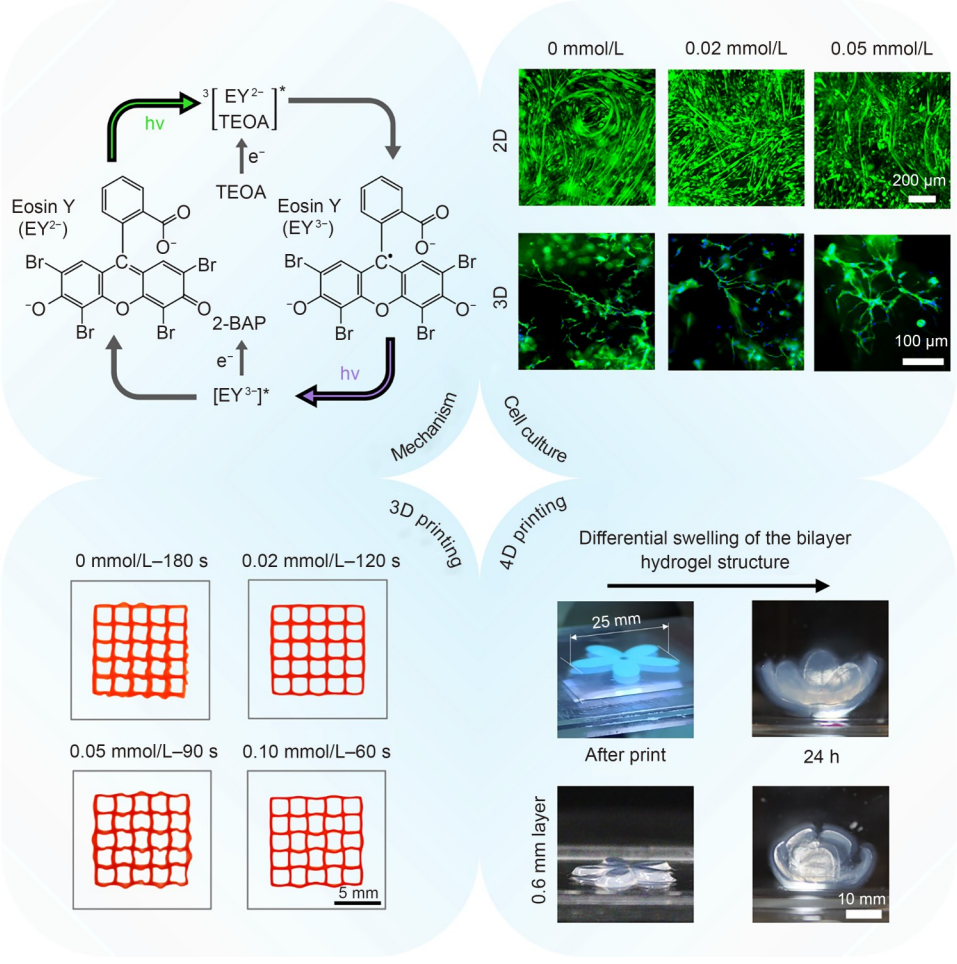

Keywords Gelatin methacryloyl (GelMA) · Bioink · Photoredox · Visible light crosslinking · Digital light processing (DLP) rapid three-dimensional (3D) bioprinting · Four-dimensional (4D) bioprinting

1 Introduction

Hydrogels have attracted considerable interest as platforms for a wide range of biomedical applications, including tissue engineering and biosensing, owing to their ability to crosslink under mild conditions. Their intrinsic biocompatibility, combined with highly tunable biochemical and physical properties, makes them excellent candidates for constructing supportive matrices in regenerative medicine and other clinical settings. Furthermore, their versatile nature enables accurate customization to replicate the biological microenvironment, facilitating targeted tissue regeneration and improved biosensor performance [1–4]. Stimuli-responsive hydrogels have attracted increasing attention for their ability to undergo structural transformations in response to environmental triggers such as light, temperature, and chemical stimuli [5, 6]. Light, including ultraviolet (UV) and visible wavelengths, is considered an ideal external stimulus for controlling hydrogel properties owing to its unique advantages. Specifically, light can (i) provide accurate on/off control, (ii) enable fine-tuning of stimulus intensity for functional modulation, (iii) achieve spatially and temporally resolved regulation of biological processes in a wavelength-dependent manner, and (iv) target well-defined regions with high accuracy [7–9]. These advantages have led to the widespread adoption of light-based techniques in biofabrication, such as stereolithography (SLA) and digital light processing (DLP) bioprinting [10, 11]. Hydrogels used in these approaches typically contain terminal or pendant alkene groups that are electron-deficient and readily undergo crosslinking reactions under photoinitiated conditions. Photocrosslinkable macromers are typically synthesized by reacting natural or synthetic polymers with methacrylation agents. This modification enables the formation of stable covalent bonds between polymer chains, resulting in a three-dimensional (3D) network upon light exposure. Representative examples of such hydrogels include polyethylene glycol diacrylate (PEGDA),

gelatin methacryloyl (GelMA), and methacrylated hyaluronic acid (MeHA) [12]. Various techniques are used to photocrosslink precursor macromer solutions into mechanically stable hydrogels, including free radical polymerization, bioorthogonal click reactions, redox-based photocrosslinking, and their combinations. Among these, light-initiated free radical polymerization remains the most widely used approach for forming covalent crosslinks between polymer chains. Its main components include precursor macromer solutions, photoinitiators, sensitizers, and light energy [13].

To induce photopolymerization or photocrosslinking in acrylated systems, two main types of photoinitiators are commonly used. The first type operates through a free radical chain mechanism, in which low-molecular-weight monomers or prepolymers absorb UV or visible light to generate highly crosslinked, chemically resistant films. This approach yields durable and solvent-resistant materials [14]. Upon irradiation at an appropriate wavelength, Type I photoinitiators absorb photons and transition to a short-lived excited triplet state, which subsequently undergoes homolytic cleavage to produce two free radicals. These radicals act as reactive species that initiate the crosslinking process in hydrogel networks. The radicals generated subsequently react with the acrylated components of the hydrogel precursor, initiating a combination of chain- and step-growth reactions that yield a stable, crosslinked polymer network. This network is essential for producing mechanically robust hydrogels suitable for biomedical applications such as tissue engineering and drug delivery [12, 15]. Among commonly used Type I photoinitiators, Irgacure 2959 is well recognized for its favorable cytocompatibility in biological systems [6, 16]. More recently, lithium phenyl-2, 4, 6-trimethylbenzoylphosphinate (LAP) has gained prominence owing to its excellent water solubility, fast polymerization kinetics, and compatibility with both UV-A (365 nm) and visible (405 nm) light sources [17]. The second class of photoinitiators functions through an ionic polymerization mechanism, most commonly cationic in nature. This approach offers key advantages, particularly its insensitivity to oxygen, and is frequently used in ring-opening polymerizations such as the curing of epoxy resins. The cationic pathway enables efficient polymerization even under oxygen-rich conditions, which can otherwise inhibit free radical processes, thereby broadening its applicability across various systems [14]. In contrast to Type I initiators, Type II photoinitiators—such as benzophenone/tertiary amine pairs—operate through a more complex initiation mechanism involving intermolecular interactions between the excited photoinitiator and a co-initiator species. In these systems, photoexcited benzophenone undergoes rapid electron transfer from the lone pair of the tertiary amine, followed by a slower proton transfer that generates the H-donor radical required to initiate polymerization [14]. However, the overall polymerization efficiency of Type II systems is generally lower than that of Type I photoinitiators, particularly in water-based applications, owing to the bimolecular nature of the process, competing back electron transfer, and the solvent cage effect in aqueous environments [14, 18]. Although the Type I photoinitiator LAP is highly water-soluble and exhibits strong molar absorptivity at 365 nm ($\epsilon \approx 200$ L/(mol·cm)), its efficiency under visible light is considerably lower, with much weaker absorptivity at 405 nm ($\epsilon \approx 30$ L/(mol·cm)) [17]. In contrast, the Type II photoinitiator eosin Y (EY) demonstrates excellent performance in the visible light range, with high water solubility and a considerably higher molar absorptivity ($\epsilon > 100\,000$ L/(mol·cm) at 515 nm), making it a more attractive option for visible-light-driven applications commonly used in biomedical applications [19].

In our previous studies, the synthesis and characterization of GelMA bioinks—including their physical and biological properties—were well established, with photocrosslinking accomplished using a complex EY-based photoinitiator system [8, 11]. While these conditions improved bioink printability, the photocrosslinking process was slower compared to UV-based systems, increasing the exposure of embedded cells to free radicals and potentially compromising cell viability. Therefore, accelerating the photopolymerization process became a priority. To address this, we developed a numerical model to simulate the physical and chemical behaviors of these bioinks and predict the progression of photocrosslinking [12]. The model also offered insights into the structural evolution of the hydrogel as crosslinking proceeded.

In this study, we evaluated the efficiency of a novel three-component photoinitiator system incorporating 2-bromoacetophenone (BAP), designed to accelerate photocrosslinking kinetics in accordance with our previously reported numerical model. The system comprised EY as the primary photosensitizer under visible light, triethanolamine (TEOA) as an electron donor and co-initiator, and BAP as a radical carrier to increase polymerization efficiency. Collectively, these components were chosen to optimize light absorption, promote rapid radical generation, and accelerate oxygen quenching during visible-light irradiation. We presented a detailed analysis of the photocrosslinking kinetics of GelMA hydrogels incorporating BAP, providing insights into intermediate reaction processes. Additionally, we demonstrated the printability of these bioinks at lower GelMA concentrations by fabricating thin structures within short time frames. Biocompatibility assessments of the resulting hydrogels were also reported. Notably, we observed a unique behavior in which BAP gradually altered the internal hydrogel structure after crosslinking. This property was leveraged to achieve four-dimensional (4D) printing of temporally assembling structures without external stimuli. Overall, our results indicate that the BAP-based photoinitiator system nearly halved both crosslinking and bioprinting times, highlighting its potential as an efficient approach for rapid hydrogel formation.

Moreover, compared to commonly used photoinitiators such as LAP, which exhibit limited absorption in the visible spectrum and therefore reduced efficiency at longer wavelengths, the BAP-based system offers distinct advantages. It enables considerably faster photocrosslinking under visible light, enhances mechanical integrity even at low GelMA concentrations, and induces unique hydration-driven structural dynamics, all while maintaining high biocompatibility, as discussed in the following sections [17].

2 Materials and methods

2.1 GelMA prepolymer preparation

GelMA was synthesized following a previously reported method with minor modifications [8]. Briefly, 5 g of porcine skin gelatin (Type A, Bloom 300, Sigma-Aldrich, St. Louis, MO, USA) was dissolved in 50 mL of distilled water at 50 °C. Upon complete dissolution, 9 mL of glycidyl methacrylate (GMA, Sigma-Aldrich) was added dropwise under continuous stirring at 750 r/min. The reaction mixture was maintained for 12 h to allow methacrylate functionalization of the gelatin, after which the solution was transferred to a dialysis membrane with a 12–14 kDa molecular weight cutoff (Fisher Scientific, Waltham, MA, USA). Dialysis was performed in distilled water for 3 d, with the water replaced twice daily. After dialysis, the GelMA solution was frozen at −20 °C for 24 h, then lyophilized for 3 d, and subsequently stored at −80 °C until further use. Prepolymer solutions were prepared by dissolving the lyophilized GelMA in phosphate-buffered saline (PBS) or distilled water, followed by the addition of photoinitiator components. The photoinitiator system consisted of various combinations of EY, TEOA, and BAP at specified concentrations.

2.2 GelMA inks with varying photoinitiator formulations

The photocrosslinking behavior was evaluated using four different photoinitiator compositions, all containing EY as the photosensitizer, TEOA as a co-initiator, and BAP as a secondary co-initiator. Control solutions were prepared with 0.02 mmol/L EY and 0.2% (w/v) TEOA, without BAP [8, 11]. The test solutions included 0.02 mmol/L EY, 0.2% TEOA, and varying concentrations of BAP. GelMA ink compositions tested in this study (Table 1) included BAP at concentrations of 0.02, 0.05, and 0.10 mmol/L, corresponding to 1×, 2.5×, and 5× the concentration of EY, respectively. Because BAP is insoluble in aqueous solvents such as PBS and distilled water, it was first dissolved in ethanol to prepare a concentrated stock solution, which was then added to the GelMA prepolymer solution to achieve the desired final photoinitiator concentrations. Hydrogels were formed by irradiating the GelMA prepolymer solutions with visible light for 300 s using a custom-made DLP bioprinting system, as described previously [8, 11].

Table 1 Compositions of GelMA inks with photoinitiators used in this study

Sample number	GelMA concentration (%)	EY (mmol/L)	TEOA (% w/v)	BAP (mmol/L)
1	5	0.02	0.2	0
2				0.02
3				0.05
4				0.10
5	7.5	0.02	0.2	0
6				0.02
7				0.05
8				0.10
9	10	0.02	0.2	0
10				0.02
11				0.05
12				0.10

2.3 Photocrosslinking assessment

The photocrosslinking behavior of GelMA inks containing the three-component photoinitiator was characterized using rheological measurements. GelMA prepolymer solutions were prepared according to the compositions listed in Table 1. For each test, 1 mL of prepolymer solution was loaded onto a rheometer (MCR 702, Anton Paar, Graz, Austria) equipped with a transparent 40 mm-diameter geometry. The light source from the custom bioprinter was positioned to project directly onto the GelMA sample through the transparent probe (Fig. S1 in the supplementary information). To ensure consistent light intensity across experiments, the distance between the light source and the GelMA sample was kept constant. The photocrosslinking assessment consisted of three consecutive measurements, following a previously reported protocol [10]. In the first measurement, the storage modulus (G') and loss modulus (G'') of the GelMA inks were recorded for 150 s with the light source turned off, taking readings every 30 s. The gap between the sample platform and geometry was maintained at 1 mm, the shear strain was set to 0.5%, and the frequency was set to 1 Hz. In the second measurement, light irradiation was applied, and the storage and loss moduli were recorded under the same settings as the first measurement. During the second measurement, data were recorded every 5 s over a total duration of 300 s. In the third consecutive test, light irradiation was turned off, and the G' and G'' of the photocrosslinked hydrogels were measured over a range of angular frequencies from 1 to 100 rad/s at a constant strain of 0.5%. All experiments were performed at an ambient temperature of 23 °C.

Slower photocrosslinking kinetics of GelMA prepolymer solutions were monitored using real-time UV–Vis spectroscopy. A transparent cuvette was filled with 700 μL of the prepolymer solution and placed in a UV–Vis spectrometer (FLAME-T-UV-VIS, Ocean Optics, FL, USA). The spectroscopy light source was aligned horizontally with the detector, while the DLP projector from the custom bioprinting system was positioned vertically, perpendicular to the UV–Vis axis, as shown in Fig. S2a (supplementary information). The projection intensity incident on the spectrometer sensor was attenuated to prevent sensor saturation. The transmitted light spectrum from the GelMA samples was recorded with a boxcar width of 20 sampling points and an integration time of 5 ms. Measurements were collected continuously over a duration of 1000 s. The DLP projector, used as the photopolymerization illumination source, was positioned 20 cm from the sample and set to an intensity of 50 mW/cm^2 to replicate a previously reported bioprinting setup [11].

2.4 Physical characterization of GelMA hydrogels

The microstructure of GelMA hydrogels was characterized using scanning electron microscopy (SEM). Prepolymer solutions containing 5% GelMA with varying BAP concentrations (0, 0.02, 0.05, and 0.10 mmol/L) were prepared. For each composition, 2 mL of prepolymer solution was dispensed into a 24-well plate and crosslinked using visible light from a DLP projection system. One set of hydrogels was immediately frozen at −80 °C after photocrosslinking, while a second set was first immersed in distilled water for 24 h to reach equilibrium swelling before freezing at −80 °C. All samples were subsequently lyophilized for 2 d. For SEM imaging, hydrogel samples were fractured vertically to expose the cross-section and mounted on aluminum stubs using carbon tape. The samples were then sputter-coated with a Pt/Pd alloy (80% Pt, 20% Pd), and microstructural images were acquired using an SEM (Mira3 XMU, TESCAN, Brno, Czech Republic). Images were processed using a custom MATLAB script, with pores manually annotated to determine average pore size and pore size distribution for each sample. For each GelMA–BAP composition, five independent hydrogel samples were prepared and imaged, capturing at least three images per sample. Pore size was quantified from more than 150 measurements per condition to ensure statistical robustness.

To assess the effect of BAP content on the water absorption capacity of GelMA hydrogels, the swelling ratio of different hydrogel samples was measured. Cylindrical constructs (8 mm diameter, 4 mm height) were prepared, washed, and blotted to determine their initial wet weights (W_w). The samples were then immersed in distilled water and maintained at room temperature in the dark for up to 24 h. At specific time points (3, 6, 9, and 24 h), the swollen hydrogels were removed, blotted, and weighed to determine their swollen weights. After measuring the swollen weights, all hydrogel samples were frozen at −80 °C and lyophilized for 3 d. The resulting dry weights (W_d) were recorded. The swelling ratio (r_s) of the hydrogels (n=5) was calculated using Eq. (1) and plotted as a function of time. Swelling behavior was characterized for hydrogels prepared with the photoinitiator compositions listed in Table 1.

$$r_s = \left(\frac{W_w - W_d}{W_d} \right) \times 100\%. \quad (1)$$

2.5 DLP printing characterization

The printing performance of the three-component photoinitiator was evaluated using a 4×4 mesh pattern under different irradiation times with 5% GelMA inks containing the photoinitiator compositions listed in Table 1. A custom vat was fabricated with a microscopic glass slide as the base and hydrophobic silicone walls. Prepolymer solutions were dispensed into the vat to achieve a layer thickness of 300 μm and a near-flat surface. The photopattern was projected onto the prepolymer solutions for different durations while keeping the distance between the projection source and the vat constant. After exposure, printed structures were developed by removing excess uncrosslinked GelMA with PBS. To visualize the otherwise transparent constructs, a red food-grade dye was used. Structures were immersed in the dye for 5 min, rinsed with PBS, and imaged using a smartphone camera. Visual assessment of structural integrity provided a qualitative comparison of printing performance. Quantitative analysis was performed using ImageJ to calculate printability (P_t) via Eq. (2) and inner arc length (ΔL), as shown in Fig. S3 (supplementary information). Additionally, a custom MATLAB script was used to measure the dimensions of mesh branches, enabling evaluation of printing resolution.

$$P_t = \frac{L^2}{16A_p}, \quad (2)$$

where L represents the perimeter and A_p represents the printed structure area.

2.6 Swelling mismatch-induced deformation (4D printing)

Two batches of 7.5% (w/v) GelMA prepolymer solutions were prepared using distilled water as the solvent. A two-component photoinitiator system (EY and TEOA) was added to the first batch, while a three-component system (EY, TEOA, and BAP) was added to the second batch, with BAP at a concentration of 0.10 mmol/L. A flower pattern (20 mm× 20 mm, convex dimensions) was first printed using the prepolymer solution without BAP, with a layer thickness of

0.6 mm. After removing uncrosslinked GelMA, the prepolymer solution containing 0.10 mmol/L BAP was added to form a second 0.6 mm-thick layer on top of the crosslinked flower pattern. The same flower pattern was projected to polymerize the second layer, aligned accurately on top of the first crosslinked layer, forming a bilayer structure with a combined thickness of 1.2 mm. Uncrosslinked prepolymer was then removed, and the samples were washed three times with distilled water before being immersed in distilled water at room temperature. The shape of the bilayer structures was monitored and imaged at various time points over 24 h. Similarly, bilayer flower structures with single-layer thicknesses of 1 and 2 mm were fabricated, and their deformation was observed during immersion in distilled water for up to 24 h.

2.7 Cell culture and biocompatibility assessment

A C2C12 mouse myoblast cell line was used to evaluate biocompatibility and cell encapsulation in 5% GelMA containing 0.02 mmol/L EY, 0.2% TEOA, and varying BAP concentrations (0.02, 0.05, and 0.10 mmol/L). Cells were cultured in Dulbecco's modified Eagle medium supplemented with 10% (v/v) fetal bovine serum and 1% (v/v) penicillin-streptomycin (PS) under a humidified atmosphere of 5% CO_2 at 37 °C. At 70%–80% confluency, cells were detached using 0.25% trypsin-ethylenediaminetetraacetic acid (trypsin-EDTA) and subcultured at a 3:1 split ratio. For experiments involving cell contact with the hydrogel surface, GelMA prepolymer solutions—including control and BAP-containing formulations—were cast into molds (10 cm diameter, 1 mm depth). Hydrogel disks were photocrosslinked for 5 min under visible light using the custom bioprinting system. The disks were then washed three times with PBS and transferred to a petri dish, where 1 mL of cell suspension (C2C12 or green fluorescent protein (GFP)-tagged NIH 3T3, 1.5×10^6 cells/mL) was gently dispensed on top. Samples were cultured in growth medium at 37 °C under 5% CO_2.

To evaluate the compatibility of the hydrogel 3D microenvironment with cells, C2C12 mouse myoblasts were encapsulated in the GelMA matrices. For 3D culture experiments, a centrifuged cell pellet was resuspended homogeneously in the prepolymer solution to prepare a bioink containing approximately 3×10^6 cells/mL. The cell-laden solution was cast into the molds described previously and photocrosslinked for 5 min. The resulting hydrogel disks were immersed in culture medium, and smaller disks (5 mm diameter) were punched out using a biopsy punch and cultured at 37 °C under 5% CO_2.

To evaluate the biocompatibility of GelMA bioinks and hydrogels containing BAP, a live/dead assay (Biotium, Hayward, CA, USA) was performed on five samples per group at Days 1, 3, 5, and 7. Cylindrical disks from 2D-cultured samples were transferred to a 6-well plate and washed three times with PBS. Samples were then incubated in live/dead assay solution, prepared by mixing 10 mL sterile PBS, 20 μL EthD-III, and 5 μL Calcein-AM, for 30 min. After incubation, samples were washed three times with PBS and imaged using an inverted epifluorescence microscope (Revolve 3, ECHO, San Diego, CA, USA). Cell viability was quantified by processing the fluorescent images in ImageJ to count live and dead cells.

Cell morphology in the different samples was assessed using cytoskeleton and nuclear staining with phalloidin (Cytoskeleton, Denver, CO, USA) and Fluoroshield with 4',6-diamidino-2-phenylindole (DAPI, Sigma-Aldrich). On Day 10, disk samples were washed three times with PBS and fixed with 4% (v/v) paraformaldehyde (Sigma-Aldrich) for 2 h at room temperature. Fixed samples were washed with PBS and permeabilized with 0.5% (v/v) Triton X-100 in PBS for 15–20 min, followed by additional PBS washes. Samples were then incubated with 100 nmol/L Phalloidin 488 to stain the cytoskeletons. After washing with PBS, samples were mounted using DAPI-containing mounting medium and imaged using a fluorescence microscope (Revolve 3, ECHO).

2.8 Statistical analysis

All quantitative data are presented as mean±standard deviation. Statistical analyses were performed using one-way analysis of variance (ANOVA) followed by Tukey's multiple comparison tests. Significance thresholds were set at $^{*}p<0.05$, $^{**}p<0.01$, $^{***}p<0.001$, and $^{****}p<0.0001$. All analyses were performed using GraphPad Prism (version 12.2.2).

3 Results and discussion

3.1 Comparison of photoinitiator formulations

Several studies have shown that visible-light-based photocuring of biopolymers offers multiple advantages, including the enhancement of the cellular microenvironment while minimizing photo-induced cytotoxicity [20–24]. Although visible-light photoinitiators such as EY have been applied in biofabrication [3, 19, 25–28], they still exhibit limitations, including oxygen inhibition, slow polymerization rates, low crosslinking density, and phase separation. Some of these challenges can be mitigated by incorporating a catalyst into the system. To optimize performance, the reaction mechanisms must be examined closely to understand the role of each component in the photocrosslinking process.

Figure 1 shows the proposed mechanisms underlying photoexcitation using EY and TEOA as photoinitiators, with 1-vinyl-2-pyrrolidinone (NVP) or BAP serving as radical carriers during polymerization [29–31]. Although the activation of EY under visible light involves a complex sequence

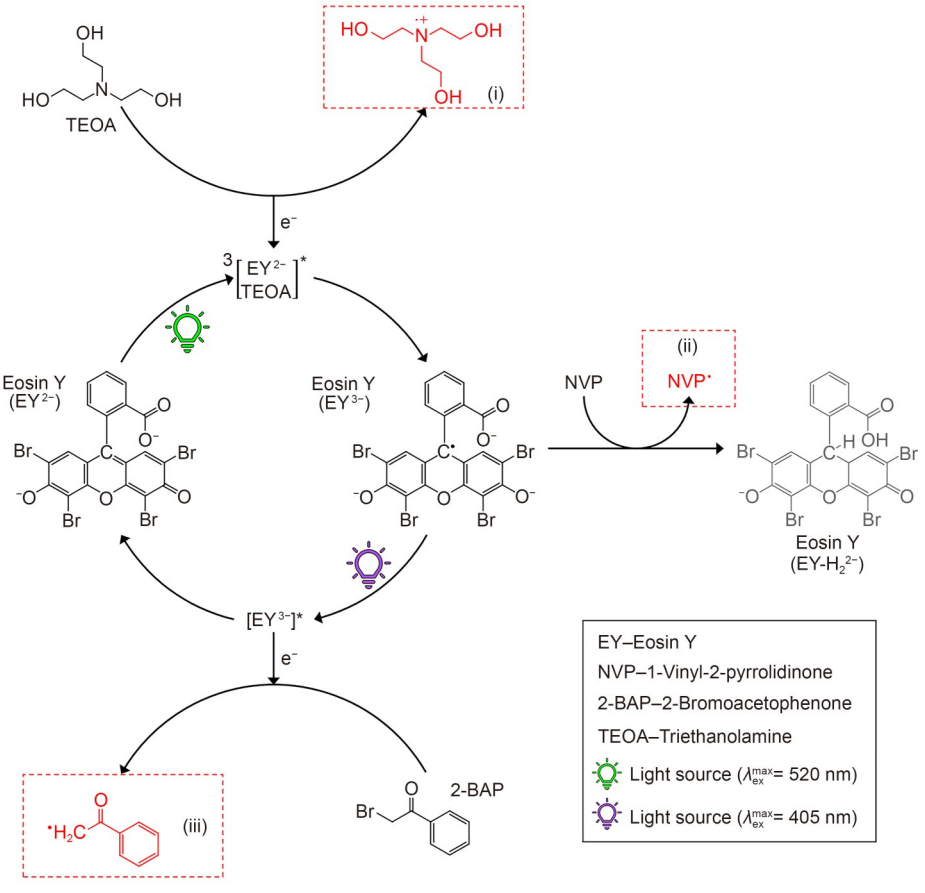

Fig. 1 Reaction mechanism of the eosin Y-based photoinitiator, illustrating the single and regenerative pathways

of electronic transitions that is not yet fully elucidated, the general mechanism is widely accepted [29–31]. Upon irradiation with green light (λ_{ex}^{max}=500 nm), EY is excited to a singlet state and rapidly transitions to a triplet state, which abstracts an electron from triethanolamine to generate the radical species $TEOA^{+}\cdot$ and $EY^{3-}\cdot$. The interaction between $TEOA^{+}\cdot$ and the methacrylate groups (−C=C−) in GelMA initiates the chain reaction required for polymerization. Meanwhile, the $EY^{3-}\cdot$ radical species is quenched by H^{+} and O_2 in the prepolymer or bioink solution, regenerating the EY catalyst and forming the reduced species $EYH^{2-}\cdot$, respectively.

Previous studies have explored the addition of NVP to the EY/TEOA system to increase the photopolymerization rate [8, 11, 32]. In this variant, the initial sequence proceeds as described above. However, the $EY^{3-}\cdot$ radical can react with the vinyl group of NVP to abstract a hydrogen atom, forming EYH_2^{2-}. Unlike the characteristic pink color of EY, this reduced species (leuco EY) appears pale green and is inactive, unable to participate in further reactions. The NVP· radical generated in this process can still promote polymerization by reacting with GelMA methacrylate groups. Importantly, this NVP radical is also susceptible to quenching by O_2, a process that depletes oxygen in the bioink and further enhances polymerization [33].

We hypothesized that a third photoactive radical pathway could be introduced by substituting NVP with BAP [29, 34]. In parallel with the photoinitiation steps described above, $EY^{3-}\cdot$ can also act as a photosensitizer: its absorption wavelength is slightly shifted toward the blue (λ_{ex}^{max}=405 nm), and its molar absorptivity at 520 nm is lower than that of EY [30]. The excited $EY^{3-}\cdot^{*}$ radical reacts with BAP in a second electron-transfer step, generating a BAP· radical and regenerating EY in its ground state, which can be resensitized by visible light. Similar to NVP, the BAP· radical can both initiate polymer chain reactions and enhance O_2 depletion in the bioink, resulting in considerably accelerated polymerization. In this photoinitiator formulation, the lifetime of the active EY photocatalyst is substantially increased, allowing the use of lower reagent concentrations.

To validate the proposed pathways, we systematically examined three photoinitiator systems and assessed their impact on crosslinking efficiency by evaluating the mechanical properties of the resulting hydrogels. Previous studies [35] demonstrated that the EY+TEOA+BAP system produced hydrogels with superior mechanical properties, higher structural integrity, and greater density compared to EY+TEOA or EY+TEOA+NVP systems. In this study, we focus on investigating both the biological and

physical properties of hydrogels formed using the EY+TEOA+BAP system.

3.2 Photopolymerization kinetics

To further investigate the effect of BAP on photocuring kinetics, rheological measurements were performed to monitor the G' and G'' of photocrosslinkable systems with varying GelMA and BAP concentrations. The analysis began with a 150 s dark phase to establish a baseline, followed by monitoring crosslinking kinetics under visible light irradiation until complete gelation. Figure 2 shows the evolution of G' and G'' over time under light exposure. Our previous numerical study [12] demonstrated that incorporating BAP into the two-component photoinitiator system (EY and TEOA) accelerated key photopolymerization steps alongside TEOA. Upon blue light irradiation, excited EY radicals ($EY\cdot^{*}$) are generated, and BAP undergoes homolytic cleavage, competing with O_2 to quench $EY\cdot^{*}$ and forming carbon-centered radicals ($R\cdot$). These $R\cdot$ radicals, together with TEOA radicals, contribute to oxygen quenching, polymer chain initiation, propagation, and network formation, ultimately accelerating photopolymerization [12, 29, 36].

Both numerical simulations and experimental results showed consistent trends. The time between the onset of light exposure and the detectable increase in G' (and G''), defined as the gelation time (GT), varied across samples. For 5% GelMA, GT values were 45, 30, 25, and 15 s for 0, 0.02, 0.05, and 0.10 mmol/L BAP, respectively, demonstrating the accelerating effect of BAP on photopolymerization (Fig. 2a; Fig. S4a in the supplementary information). However, in the 7.5% and 10% GelMA groups, the difference in GT across BAP concentrations was less pronounced (Fig. 2b; Figs. S4b and S4c in the supplementary information). This is likely

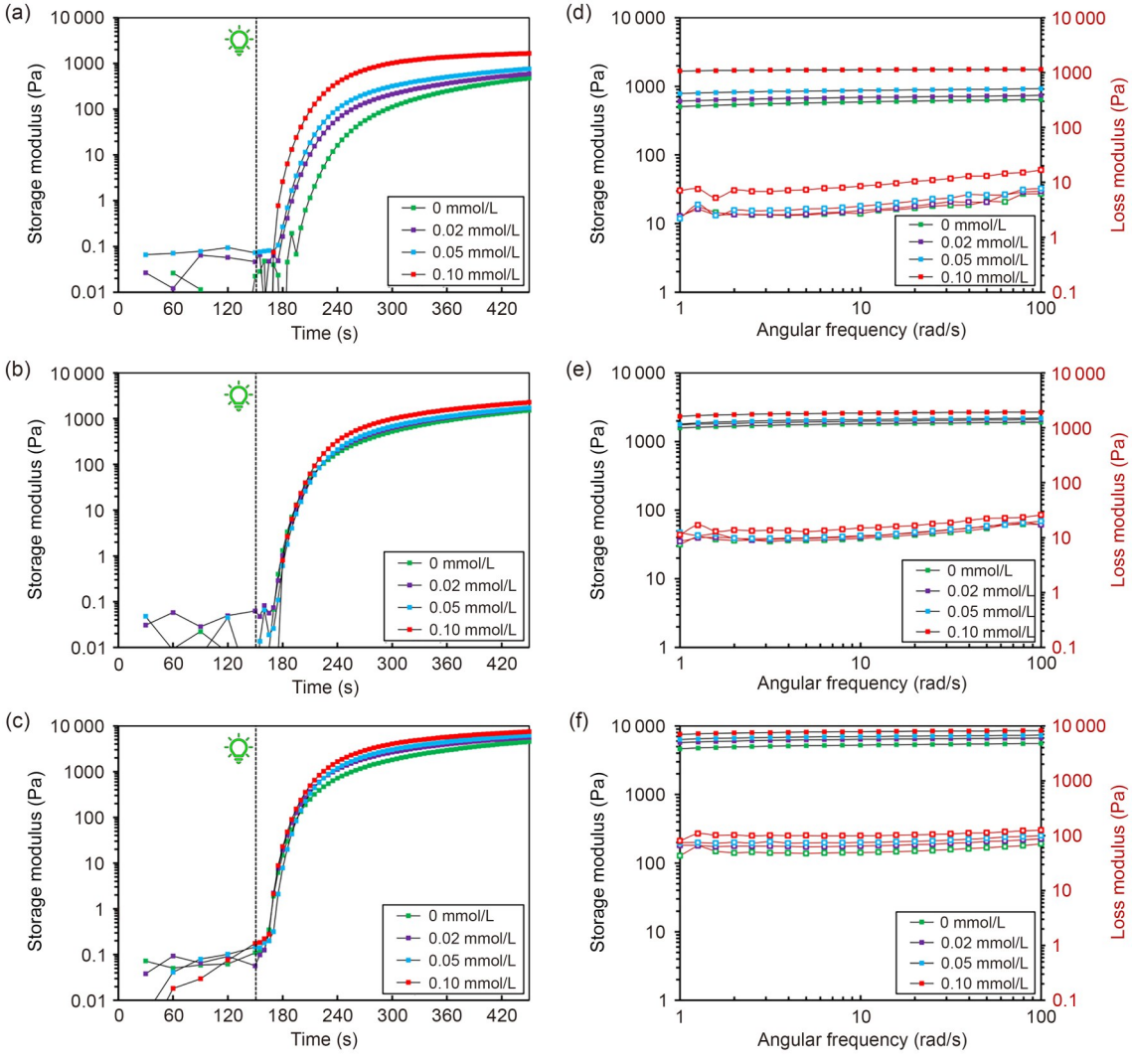

Fig. 2 Photocrosslinking kinetics of GelMA. Real-time monitoring of the storage modulus during crosslinking of 5% GelMA (a), 7.5% GelMA (b), and 10% GelMA (c) containing 0, 0.02, 0.05, and 0.10 mmol/L BAP. Frequency sweep analysis of 5% GelMA (d), 7.5% GelMA (e), and 10% GelMA (f) with the same BAP concentrations. Storage modulus: black line with solid-filled markers; loss modulus: red line with open markers

attributed to the higher GelMA concentration, which increases the density of methacrylate groups and shortens the free radical diffusion path, thereby reducing the influence of BAP on GT.

Increasing BAP concentration enhances the generation of R· radicals, leading to a higher degree of methacrylate group conversion and, therefore, increased crosslinking density. As a result, higher BAP concentrations produce stiffer hydrogels. As shown in Fig. 2a and Fig. S4a (supplementary information), among the 5% GelMA samples, the 0.10 mmol/L BAP hydrogel exhibited the highest saturated G' and G'' values after reaching the plateau, indicating the formation of a fully crosslinked gel structure. For 7.5% and 10% GelMA, the overall mechanical stiffness was higher owing to the increased polymer concentration, resulting in greater G' and G'' values compared to 5% GelMA. Although Figs. 2b and 2c and Figs. S4b and S4c show a similar increasing trend in G' and G'', the variations in each 7.5% and 10% GelMA group were less pronounced than those observed in the 5% GelMA samples.

Furthermore, the viscoelastic behavior of the crosslinked gels was analyzed and is presented in Figs. 2d–2f. In all samples, G' remained higher than G'', confirming the gel-like behavior of the hydrogels. Both G' and G'' were largely independent of angular frequency across all formulations, indicating the formation of a fully crosslinked network. As GelMA concentration increased, both moduli increased for all BAP concentrations (Figs. 2d–2f). Furthermore, in each GelMA group, higher BAP concentrations resulted in additional increases in G' and G'', reflecting enhanced stiffness owing to a higher degree of crosslinking (Figs. 2d–2f).

To demonstrate the versatility of BAP across different photocrosslinkable hydrogels, PEGDA was selected as a representative synthetic system. A 30% (w/v) PEGDA solution required a twofold increase in EY and TEOA concentrations to achieve effective crosslinking [37]. Accordingly, all PEGDA formulations were prepared with 2× EY and TEOA, while BAP was added at the same concentrations used for GelMA and at double concentrations to maintain consistent photoinitiator ratios. As shown in Fig. S5 (supplementary information), incorporation of BAP at both concentration levels accelerated the crosslinking rate (steeper initial slope of storage modulus increase) and increased the final storage modulus. These trends were consistent with those observed in GelMA, confirming that the effect of BAP extends beyond natural polymers.

To further investigate the effect of BAP on the photocrosslinking initiation rate of GelMA, four bioink compositions were tested with BAP concentrations of 0.02, 0.05, and 0.10 mmol/L, corresponding to 1×, 2.5×, and 5× the EY concentration, respectively, and were compared to a control containing 0 mmol/L BAP. Based on the rheological results, which showed the greatest variation among BAP concentrations in 5% GelMA, this concentration was selected for further analysis using UV–Vis spectroscopy. The other photoinitiator components (EY and TEOA) were kept constant across all formulations. The UV–Vis experimental setup is shown in Fig. S2a (supplementary information). Figure S2b (supplementary information) shows the color changes that occur during photopolymerization: Fig. S2b-(1) shows the prepolymer solution before visible light irradiation; Fig. S2b-(2) depicts the photoinitiator (EY+TEOA+BAP) after continuous visible light exposure; Fig. S2b-(3) shows the translucent appearance of the fully photocrosslinked hydrogel.

Real-time UV–Vis spectroscopy coupled with in situ photopolymerization revealed clear differences in photopolymerization rates among the bioink compositions. The rate of photocrosslinking increased with higher BAP concentrations. To quantify this, the initial slope of the crosslinking kinetic curves was evaluated as a representative measure of the photopolymerization rate. An average slope was calculated to account for the concave and convex regions in the kinetic curves. The observed slopes were 0.60 (31.13°), 1.21 (50.54°), 1.90 (62.20°), and 2.42 (67.61°) for 0, 0.02, 0.05, and 0.10 mmol/L BAP, respectively (Fig. 3a). As BAP concentration increased from 0 mmol/L, the slope of the polymerization kinetics rose sharply and approached a plateau near 0.10 mmol/L BAP. The rate of increase in polymerization speed was not proportional to BAP concentration, saturating at higher levels (Fig. 3b). This could be a result of rapid consumption of TEOA, making it the rate-limiting species.

Figure 3 compares different regions of the photopolymerization kinetics curves. The regions highlighted in red, green, and black correspond to the acceleration, deceleration, and saturation phases of photopolymerization, respectively. Figure 3b shows the first derivative of the polymerization kinetics curves, with the largest magnitude observed for 0.10 mmol/L BAP, indicating the fastest instantaneous polymerization rate among all compositions. The second derivative, shown in Fig. 3c, represents the acceleration and deceleration of polymerization. As previously discussed, oxygen quenching competes with these reactions, contributing to a pronounced slowdown in polymerization during certain phases. The magnitude of the second derivative in the acceleration region can be correlated with the rate of oxygen depletion in the bioink layer [38–41]. Bioinks with higher BAP concentrations deplete oxygen more rapidly, allowing the various reactions to contribute to polymer formation sooner. Examination of the transition in the second derivative curve from positive to negative slope indicates the point at which polymerization shifts from the acceleration to deceleration phase for each BAP concentration. Beyond this transition, polymerization is likely governed by other factors, such as the diffusion of chemical species in the bioink and BAP, a process that slows the overall reaction rate.

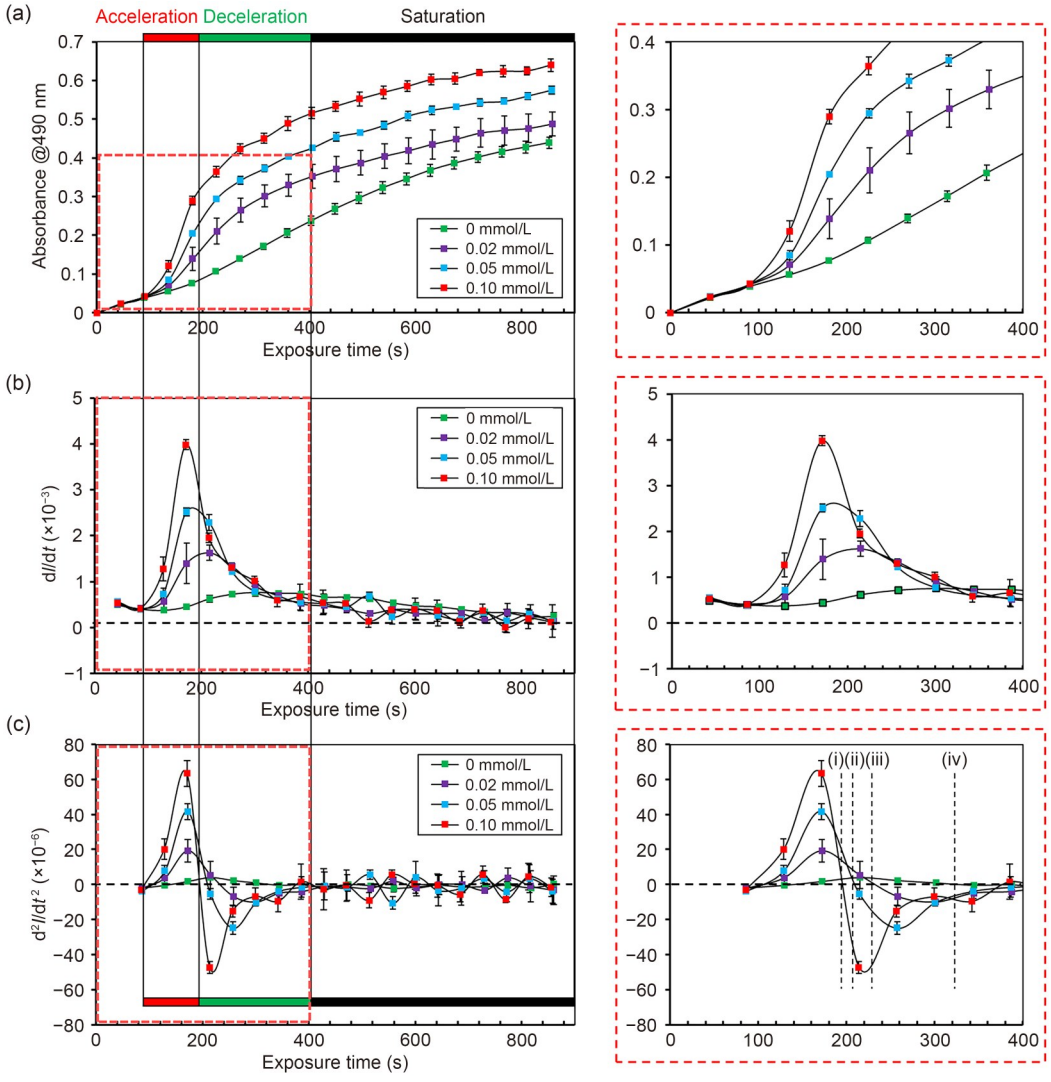

Fig. 3 Photocrosslinking kinetics of GelMA with a three-component photoinitiator. (a) Polymerization kinetics curves recorded by measuring absorbance at 490 nm, showing the slopes corresponding to different BAP concentrations and distinct regimes of crosslinking kinetics (acceleration, deceleration, and saturation). (b) First derivative of the kinetics curves representing the polymerization rate. (c) Second derivative of the kinetics curves representing polymerization acceleration. The acceleration-to-deceleration transition points for different bioinks are marked as (i) 0.10 mmol/L BAP, (ii) 0.05 mmol/L BAP, (iii) 0.02 mmol/L BAP, and (iv) 0 mmol/L BAP. Data are expressed as mean±standard deviation (n=3)

3.3 Physical characteristics

We next examined the internal structure of the photocrosslinked GelMA hydrogels obtained from bioinks with different BAP concentrations. Figure 4a shows representative SEM images of the internal porous microscale structure of the hydrogels. Analysis of the SEM images revealed an increasing trend in pore size with higher BAP concentrations (Figs. 4a and 4b). This effect may arise from several factors that warrant further investigation. BAP is hydrophobic, whereas GelMA is predominantly hydrophilic owing to its gelatin backbone. During gelation, this incompatibility could induce microphase separation, with BAP-rich hydrophobic regions segregating from the surrounding hydrophilic polymer matrix [42, 43]. The presence of BAP also accelerates oxygen depletion through additional oxygen-quenching reactions. In free radical polymerization, oxygen reacts with free radicals generated by the photoinitiator (EY), forming less reactive peroxy radicals. These peroxy radicals can terminate chain growth, reducing the overall crosslinking efficiency. In low-oxygen or oxygen-depleted conditions, a greater proportion of free radicals participate in polymerization, resulting in higher crosslinking density [12]. Therefore, increasing BAP concentration can considerably accelerate photopolymerization compared to previous reports [12]. While faster polymerization increases the overall degree of crosslinking, it can also trap microdomains or bubbles in the hydrogel matrix before the network fully equilibrates, limiting uniform polymer chain rearrangement. This promotes localized phase separation, with the resulting microdomains manifesting as larger pores in the

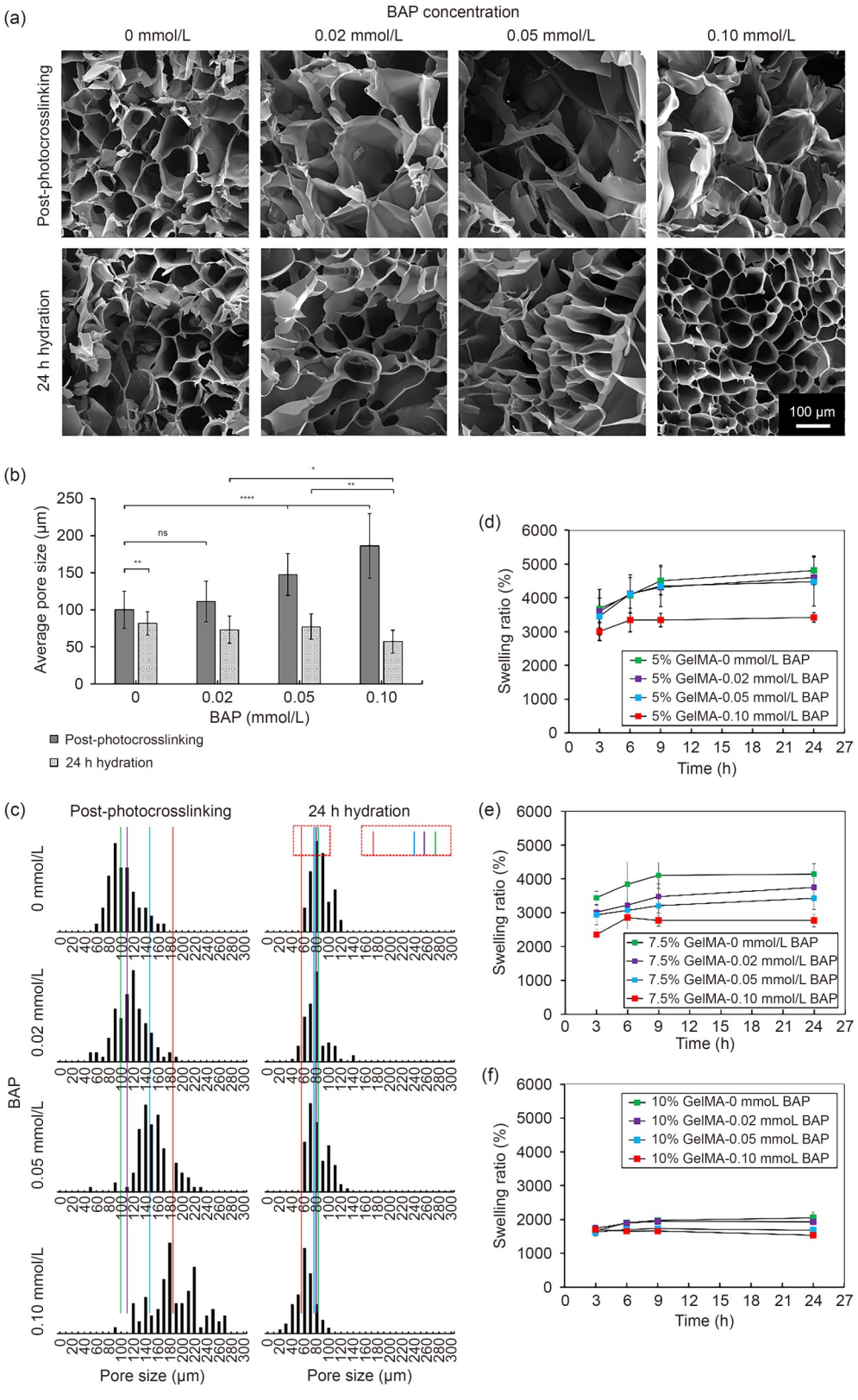

Fig. 4 Microstructural and swelling analysis of GelMA hydrogels with varying BAP concentrations. (a) Representative SEM images showing the internal pore structure. (b) Average pore size measured from SEM images (n=5) before and after swelling. (c) Pore size distribution, where green, purple, blue, and red lines indicate the average pore sizes of 5% GelMA samples containing 0, 0.02, 0.05, and 0.10 mmol/L BAP, respectively, both after photocrosslinking and following 24 h of hydration. Swelling ratio profiles for 5% (d), 7.5% (e), and 10% (f) GelMA containing 0, 0.02, 0.05, and 0.10 mmol/L BAP. Data are expressed as mean±standard deviation (n=3). $^{*}p<0.05$, $^{**}p<0.01$, and $^{****}p<0.0001$; ns: not significant

final structure [44]. Figure 4c shows that at the highest BAP concentration, the pore size distribution is broader compared to samples without BAP or with lower BAP concentrations.

During hydration, the photocrosslinked hydrogels exhibited noticeable shrinkage over time. To investigate this behavior, 5% GelMA hydrogels with varying BAP concentrations were photocrosslinked and incubated in distilled water at room temperature for 24 h. Distilled water was used to eliminate the influence of ionic interactions. SEM images of the internal porous structure after 24 h of hydration are shown in Fig. 4a. Analysis of the images revealed a considerable reduction in average pore size compared to samples lyophilized immediately after photopolymerization, indicating structural rearrangements during swelling (Fig. 4b). In samples without BAP, only a slight decrease in average pore size was observed after 24 h of immersion in distilled water, and the pore size distribution largely overlapped with that of the post-photocrosslinked hydrogels (Fig. 4c). With increasing BAP concentration, the reduction in average pore size after 24 h became more pronounced compared to post-photocrosslinking samples (Fig. 4b). Additionally, higher BAP concentrations resulted in a more uniform internal porous structure after hydration, as evidenced by the narrower pore size distributions in Fig. 4c. Among the 24-h hydrated samples, the average pore size decreased with increasing BAP concentration, indicating that BAP influences the internal pore structure over time and contributes to overall hydrogel shrinkage. Shrinkable hydrogels [45] are a class of materials that deswell or contract in response to external stimuli such as temperature [46], pH [47], ionic composition [48], or solvent exchange, and they have been explored for various biomedical applications, including wound healing [48], drug delivery [49], and tissue engineering [50, 51]. For example, Fang et al. [48] reported a chitosan-based hydrogel for wound healing that shrank in PBS owing to ionic interactions between the hydrogel and ions in the solution, leading to a gradual reduction of the wound area. However, the exact mechanism underlying this behavior in BAP-containing GelMA remains to be elucidated in future studies. One potential explanation for the reduced swelling is secondary crosslinking over time, where residual reactive groups in GelMA or BAP continue to form additional crosslinks even after the initial gelation process. Prolonged exposure to water can enhance molecular mobility, allowing residual methacrylate groups to react and form new covalent bonds, thereby tightening the hydrogel network. Structural relaxation and network reorganization during extended hydration may also contribute to the observed shrinkage [52]. The polymer network of the hydrogel may undergo relaxation and rearrangement during prolonged hydration. During swelling, the polymer chains can reorganize into more energetically favorable configurations. This structural relaxation often results in network contraction and a reduction in pore size. Such shrinkage and pore size reduction influence the swelling behavior of the hydrogels.

The swelling behavior of the hydrogels was assessed by incubating them in distilled water at room temperature for 24 h, with results shown in Figs. 4d–4f. As GelMA concentration increased, the density of methacryloyl groups increased, leading to a higher degree of crosslinking. This resulted in stiffer structures with smaller pores and therefore lower swelling ratios (Figs. 4d–4f) [53, 54]. Across all GelMA formulations, increasing BAP concentration further reduced the swelling ratio, likely owing to the hydrophobic nature of BAP, which introduces water-repelling regions in the hydrogel network (Figs. 4d–4f). The reduction in pore size with increasing GelMA concentration, along with prior structural analyses, indicates that hydrogel shrinkage occurs during hydration, resulting in decreased pore sizes. Therefore, at lower GelMA concentrations (Fig. 4d), the difference in swelling ratios between 3 and 24 h is more pronounced. In contrast, at higher GelMA concentrations (Fig. 4f), minimal pore size changes occur during hydration, leading to smaller differences in swelling ratios over the same time period.

Furthermore, as shown in Fig. 4d, hydrogels containing 0, 0.02, and 0.05 mmol/L BAP did not reach a plateau in swelling behavior in 24 h, whereas the sample with 0.10 mmol/L BAP achieved equilibrium. This difference may be attributed to the similar pore sizes observed in hydrogels with 0, 0.02, and 0.05 mmol/L BAP after hydration, whereas the 0.10 mmol/L BAP hydrogel exhibited a substantially larger pore size, as evident in Figs. 4a and 4b.

For 7.5% and 10% GelMA combinations (Figs. 4e and 4f), samples with a high BAP concentration (0.10 mmol/L) exhibited a decreasing trend in swelling ratio after 24 h compared to other BAP concentrations. This behavior is likely attributed to the already low swelling ratios in these samples, resulting from their smaller pore sizes, which are further reduced by the high BAP content. The additional pore size reduction may promote water release and partial dehydration of the hydrogel over time. Similar shrinkage of photocrosslinked structures has also been frequently observed in SLA-printed parts using acrylate resin formulations.

3.4 Printing capability evaluation

Rapid photopolymerization kinetics are critical for light-based (bio)printing because they directly influence the resolution and structural fidelity of printed constructs. To evaluate this, a 1 cm×1 cm mesh pattern was printed using 5% GelMA bioinks with varying BAP concentrations. Given the soft and mechanically weak nature of 5% GelMA hydrogels, the effect of BAP on crosslinking efficiency and printability was specifically assessed. For bioinks without BAP, no printing was observed at exposure times shorter than 150 s (Fig. 5a). At 150 s of exposure, a fragile structure formed, but the mesh

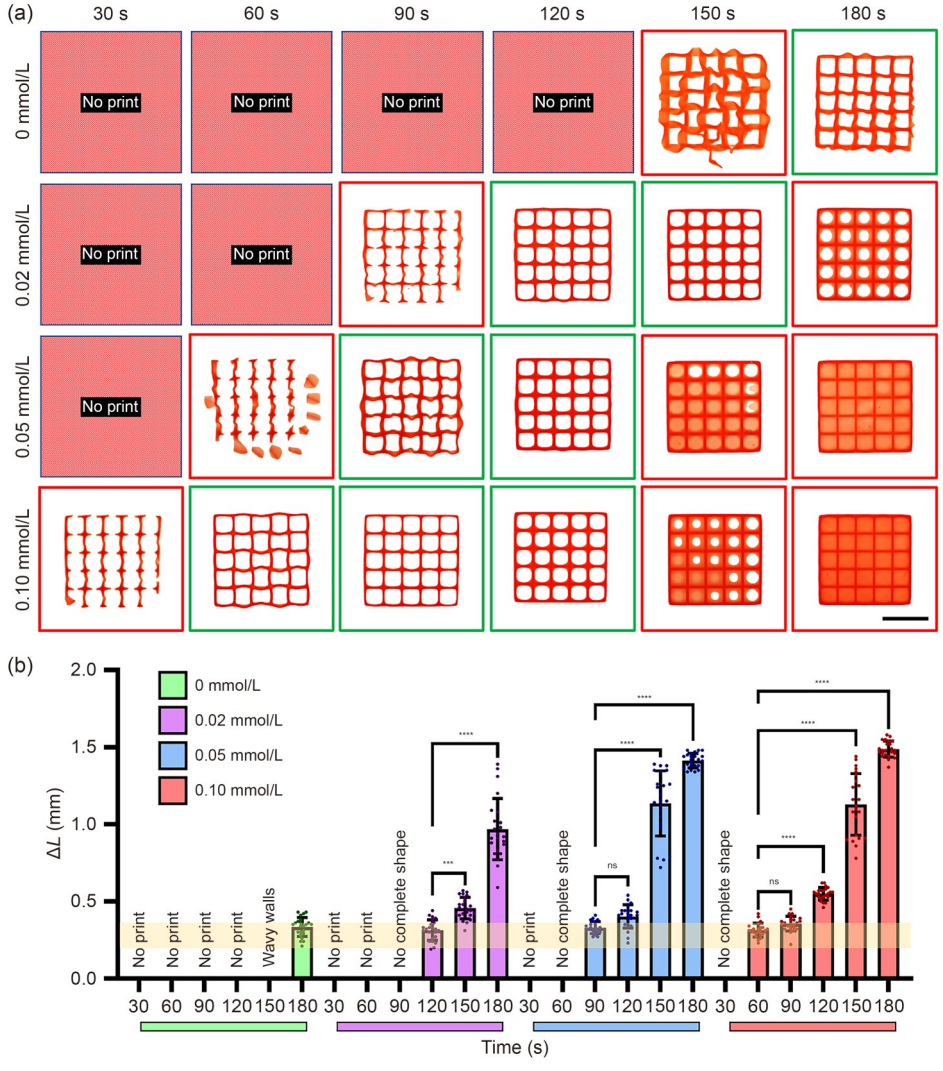

Fig. 5 Light-based printing evaluation. (a) Photopatterning of 5% GelMA containing 0, 0.02, 0.05, and 0.10 mmol/L BAP under different light irradiation durations (scale bar: 5 mm). (b) Measurement of the inner arc length (ΔL) under various photocrosslinking conditions. Data are expressed as mean±standard deviation ($n \geq 3$). $^{***}p<0.001$ and $^{****}p<0.0001$; ns: not significant

walls remained unstable, wobbling under media movement. Increasing the exposure time to 180 s produced a more stable structure; however, the walls were still wavy and irregular. Despite these instabilities, the printability (P_t) values approached the acceptable range (Fig. S6 in the supplementary information), and the inner arc length closely matched the designed light pattern (Fig. 5b).

With the addition of 0.02 mmol/L BAP, exposure times of 30 and 60 s did not yield crosslinked structures. Partial crosslinking occurred at 90 s, but some mesh connections remained broken or disconnected. A stable structure with clearly defined lines was achieved at 120 s (Fig. 5a), with ΔL values falling within the acceptable crosslinking range. At this exposure time, the average crosslinked line thickness closely matched the projected light beam thickness on the precured GelMA, indicating optimal crosslinking (Fig. S7 in the supplementary information). However, further increasing the exposure time to 150 s and beyond caused overcrosslinking, resulting in polymerization in the voids and surrounding regions (Fig. 5a). At 180 s exposure, the void regions of the design were completely crosslinked, with ΔL considerably exceeding the values in successfully crosslinked conditions (Fig. 5b). Figure S7 (supplementary information) shows that at both 150 and 180 s, the line thickness exceeded the projected light beam width. Although P_t values remained relatively stable across all structures in the 0.02 mmol/L BAP group, a slight decrease with increasing exposure time indicated a decline in printing fidelity owing to overcrosslinking (Fig. S6 in the supplementary information).

With 0.05 mmol/L BAP, partial structures formed after 60 s exposure but lacked sufficient strength to maintain their intended shape, exhibiting distorted, wavy branches (Fig. 5a). A more stable, fully formed structure appeared at 90 s, although slight waviness persisted in the branches (Video S1

in the supplementary information). At 120 s, a firm, well-defined mesh was successfully printed. Both 90 and 120 s exposures produced ΔL values within the desirable crosslinking range (Fig. 5b). However, exposure times of 150 s and beyond caused extensive overcrosslinking, polymerizing the surrounding regions. Although printability remained within or near the acceptable range for 90 and 120 s, Fig. S6 (supplementary information) shows that increasing crosslinking time led to a decrease in P_t, reflecting overcrosslinking in the mesh voids.

For bioinks containing 0.10 mmol/L BAP, partial crosslinking was already observed after 30 s of irradiation, highlighting the accelerated photopolymerization in the presence of BAP. A well-resolved structure with stable, distinguishable branches was achieved at 60 s, while 90 s exposure resulted in rigid mesh walls. As shown in Fig. 5b, ΔL values remained within the acceptable range. Moreover, both 60 and 90 s exposures produced average line thicknesses consistent with the projected light beam, indicating accurate and controlled crosslinking (Fig. S7 in the supplementary information). Exposure durations of 120 s or longer caused excessive crosslinking, considerably increasing ΔL beyond the optimal range. While the increase in ΔL indicated overcrosslinking in the void regions of the mesh pattern, the line thickness stayed within acceptable limits, indicating controlled crosslinking in the patterned areas (Fig. S7 in the supplementary information). In addition to ΔL, P_t values were assessed, revealing that for exposure times exceeding 90 s, P_t steadily decreased owing to overcrosslinking in the void spaces of the mesh pattern (Fig. S6 in the supplementary information).

As reported in the photocrosslinking kinetics characterization, increasing the concentration of BAP in the photoinitiator system accelerates the polymerization rate. This is further confirmed by the reduced exposure time needed to form a stable structure with higher BAP concentrations (Fig. 5a). During photocrosslinking of GelMA bioinks using a three-component photoinitiator, a sequence of intermediate reactions takes place. These reactions are heavily influenced by oxygen, which quenches reactive species and slows polymerization, as well as by the diffusion of generated free radicals [55]. In the bioprinting of small structures, slower photopolymerization allows greater diffusion of chemical species, which can reduce printing resolution by causing structure blurring or less accurate feature formation. Conversely, faster polymerization limits species diffusion, ensuring sharper and more defined structures. Rapid photopolymerization also depletes oxygen in the bioink layer, reducing the quenching of intermediate reactive species and thereby enhancing polymerization efficiency. Moreover, faster bioprinting minimizes the exposure of encapsulated cells to harmful free radicals, which improves cell viability and the biocompatibility of the printed constructs.

To further improve printing accuracy, a pulsed projection strategy for the photopattern was used. Our previous numerical study [12] demonstrated that pulsed illumination, compared to continuous exposure, considerably enhanced the resolution of hydrogel-printed structures. Under continuous illumination, rapid polymerization causes overcrosslinking in adjacent areas, which reduces printing accuracy and fidelity. In contrast, pulsed exposure slows down excessive crosslinking in non-targeted regions, preserving structural accuracy across the hydrogel width. This improvement is primarily attributed to rapid oxygen depletion during continuous exposure, while pulsed illumination allows oxygen to replenish between pulses, effectively regulating polymerization and improving print quality. Oxygen replenishment during pulsed photocrosslinking increases the quenching of a larger number of intermediate species, including those that diffuse outside the illuminated area. This reduces radical-driven overcrosslinking in regions with fewer radicals, improving spatial control of hydrogel formation [12]. Compared to continuous exposure, pulsed photocrosslinking offers better resolution, enhanced mechanical property control [56], reduced light-induced cytotoxicity, and optimal light dosing. These advantages make pulsed illumination an effective strategy for producing high-fidelity, structurally stable, and biocompatible hydrogel constructs.

To examine the effect of pulsed light on the resolution of printed GelMA hydrogels, two high concentrations of BAP (0.05 and 0.10 mmol/L) were chosen owing to their faster crosslinking kinetics. Structures were fabricated under two different photocrosslinking conditions—continuous and pulsed exposure (20 frames per second). Figure S8 (supplementary information) shows the results after 120 s of photocrosslinking. Under continuous light irradiation, hydrogels containing 0.05 and 0.10 mmol/L BAP achieved the desired degree of crosslinking, with the average line thickness of the printed structures closely matching the width of the light beam. However, under pulsed photopattern projection, the average line thickness of the printed constructs was substantially reduced to approximately 375 and 475 μm for GelMA containing 0.05 and 0.10 mmol/L BAP, respectively. In both cases, the printed lines were approximately one-third the width of the projected light beam (approximately 1000 μm), demonstrating the accuracy-enhancing effect of pulsed illumination. Despite the reduced line width in the printed constructs, no waviness or instability was observed, unlike in the undercrosslinked structures shown in Fig. 5a. This confirms the stability of the printed constructs obtained with pulsed projection and attributes the higher printing resolution to accurate control of the photocrosslinking kinetics.

3.5 4D printing: water-triggered deformation

Creating composite structures with mismatched or differential swelling behavior is a widely used strategy for enabling programmable deformation, thereby expanding the capabilities of

4D-printed polymers [57–59]. To achieve structural movement using smart hydrogels, the printed constructs must satisfy two key criteria: (i) they should contain regions with varying swelling capacities to generate stress distribution during swelling or exhibit directional swelling differences; (ii) they must be able to absorb and release solvents, allowing the materials to undergo swelling and deswelling [59]. Based on observations of changes in the internal porous structure and shrinkage of GelMA hydrogels with BAP, along with the swelling profiles of different GelMA–BAP combinations, a bilayer structure with a flower pattern was designed and fabricated. Owing to the pronounced differences in swelling behavior among the various BAP concentrations in the 7.5% GelMA group, this concentration was chosen for the swelling-induced deformation study. As shown in Fig. 4b, the extent of pore size reduction was greatest for 0.10 mmol/L BAP hydrogels and smallest for 0 mmol/L BAP hydrogels.

The bottom layer of the flower pattern was fabricated with 7.5% GelMA using EY+TEOA photoinitiators (Fig. 6), while the top layer was made from 7.5% GelMA containing EY+TEOA+0.10 mmol/L BAP. Upon hydration of the bilayer structure in distilled water after fabrication, the structure bent upwards (Fig. 6). The baseline of the printed structures is highlighted in yellow to clearly visualize the deformation of the bilayer.

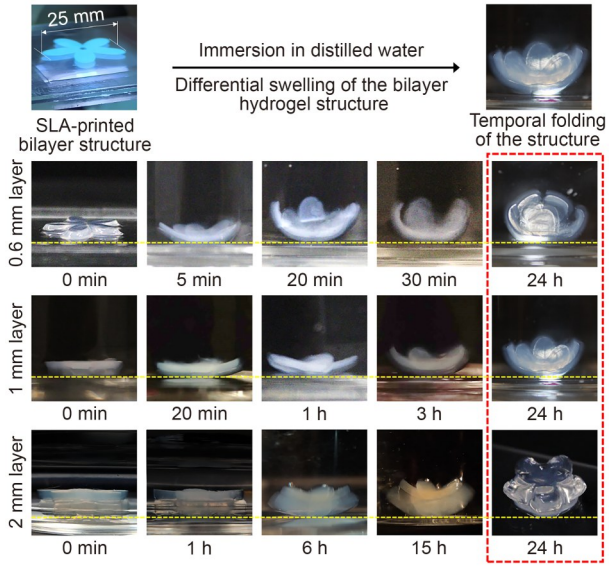

Fig. 6 Swelling-induced shape transformation of printed hydrogel structures with different layer thicknesses. The top-left image shows the initial 3D-printed structure (25 mm in diameter) before swelling. Sequential images depict the time-lapse deformation of structures with varying layer thicknesses (0.6, 1, and 2 mm) under swelling conditions

Structures with different layer thicknesses were printed to assess the controllability of shape morphing. Figure 6 shows the deformation progression of each structure over 24 h, and Video S2 (supplementary information) provides a time-lapse of the deformation process for the 0.6 mm layer thickness structure over 20 min. To quantify the degree of deformation, the deflection angle of the highest point of the flower-like structure was measured relative to the base layer, as shown in Fig. S9 (supplementary information). The results indicate that thinner printed layers undergo greater deformation. For the 0.6 mm layer thickness, the structure reached a deflection angle of θ=104.12°±11.95° within 30 min. In comparison, structures with 1 and 2 mm layer thicknesses exhibited considerably lower deflection angles of θ=38.43°±2.55° and θ=14.67°±0.92°, respectively, after 1 h of swelling. After 24 h, the 0.6 mm layer thickness showed the greatest deformation, with the petals folding inward toward the center and reaching a final deflection angle of θ=125.46°±8.63°. This deformation exceeded that observed in the 1-mm-thick and 2-mm-thick layer structures.

As described earlier, the addition of BAP led to a decrease in the average pore size of the hydrogels during hydration. When the bilayer structure was immersed in distilled water, the top layer experienced greater shrinkage compared to the bottom layer, causing a differential swelling ratio that resulted in the gradual bending of the structure. This phenomenon confirmed the feasibility of programmed deformations driven by swelling mismatch. This finding emphasizes the potential applications of these hydrogels in origami-inspired programmed deforming structures [60] and drug delivery systems [61].

3.6 Biocompatibility characterization

A preliminary evaluation of the biocompatibility of hydrogels prepared with BAP was performed using 5% GelMA and the C2C12 mouse myoblast cell line cultured on the surface of the crosslinked hydrogels. Initially, hydrogel disks were fabricated with varying photoinitiator formulations—0.02 mmol/L EY+0.2% TEOA+x mmol/L BAP (x: 0, 0.02, 0.05, and 0.10). Live/Dead assays were performed at 1, 3, 5, and 7 d after seeding the cells on the hydrogel surfaces. Figure 7a shows representative fluorescence images stained with Calcein-AM (green) for live cells and propidium iodide (red) for dead cells. Cell viability quantified from these images exceeded 97% across all formulations during the first week (Fig. 7b), thus demonstrating the biocompatibility of the hydrogels formed using BAP.

After 24 h of seeding on the hydrogel surface, C2C12 cells adhered and spread across it, predominantly retaining a round shape or showing limited elongation in certain areas. By Day 3, these cells fused to form chains, and by Day 5, myogenic differentiation was evident, with myotubes visible throughout most of the hydrogel surface. To confirm both the differentiation and morphological changes, C2C12 cells cultured on the hydrogels were stained for myosin heavy chain (MyoHC), a specific molecular marker indicating myotube formation.

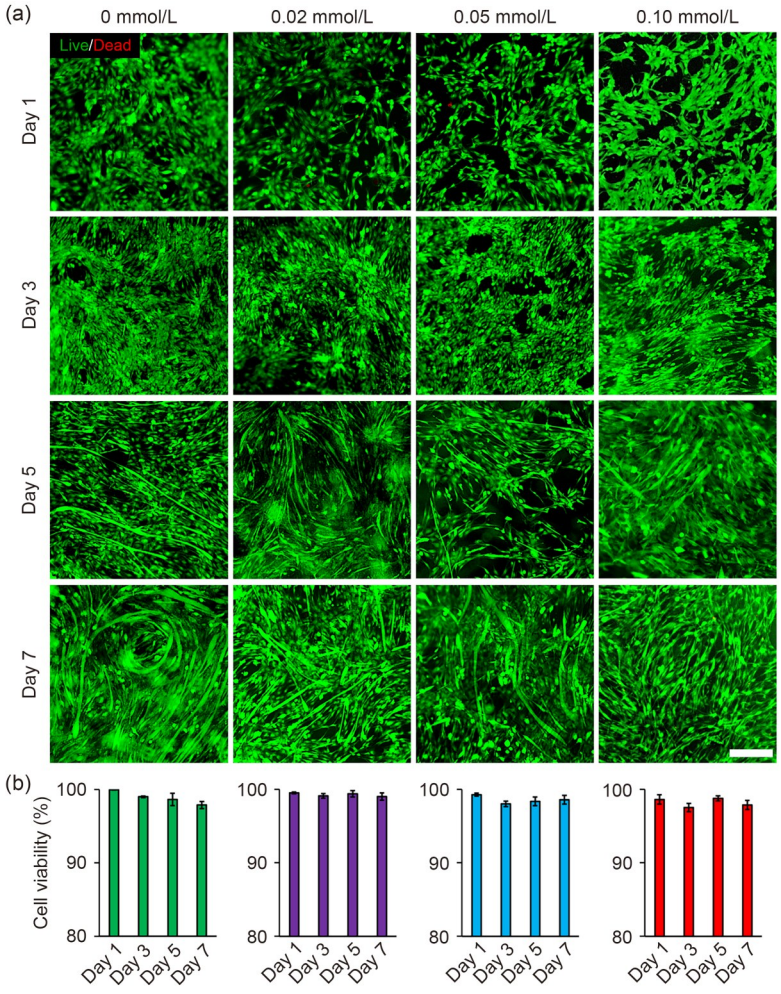

Fig. 7 Live/Dead assay of C2C12 myoblasts cultured on crosslinked hydrogel surfaces. C2C12 cells were grown as 2D monolayers on various crosslinked hydrogels. (a) Live cells appear green, and dead cells appear red, showing cell viability across different hydrogel conditions (scale bar: 200 μm). (b) Quantitative analysis of C2C12 cell viability over 7 d of culture. Data are expressed as mean±standard deviation (n=3)

The presence of MyoHC-positive multinucleated fibers confirmed that myogenic differentiation occurred in the BAP-containing hydrogels, aligning with the cytoskeletal patterns seen in phalloidin/DAPI staining (Fig. S10 in the supplementary information). Additionally, live/dead assay results demonstrated that C2C12 myoblast proliferation and differentiation were effectively promoted across all biomaterial groups, including both the control GelMA hydrogel and those with BAP.

Moreover, to further assess biocompatibility with a different cell type, NIH 3T3 fibroblasts were seeded onto the hydrogels. After 7 d of culture, cell viability exceeded 90% in all formulations (Fig. S11 in the supplementary information). These findings confirm that the BAP-based photoinitiator system is compatible with multiple mammalian cell types.

The essential role of cells in adhesion, spreading, and growth on hydrogels is critical for tissue development [62, 63]. To evaluate proliferation, morphology, and distribution in the composites, immunofluorescence staining of F-actin and nuclei (phalloidin and DAPI) was performed after 10 d of culture. Figure 8 shows cell spreading in the hydrogels. In formulations with less than 0.10 mmol/L BAP, C2C12 cells showed elongation, which was linked to abundant mature focal adhesions, assembly of F-actin filaments, and an interconnected cytoskeletal network along cell chains. In 3D scaffolds, matrix stiffness and porosity critically influence proliferation, cell spreading, and migration. The formation of stiffer hydrogels in the presence of BAP promoted the development of mature focal adhesions between myoblasts and the scaffold matrix because myoblasts favor such stiffer microenvironments. However, this effect was not observed in the sample with 0.10 mmol/L BAP owing to an excessive increase in hydrogel stiffness. Rheological analysis showed that the 0.10 mmol/L BAP sample had the highest stiffness compared to other formulations (Fig. 2). The hydrogels formed with 5% GelMA and those containing 0.02 and 0.05 mmol/L BAP did not exhibit striking differences in their stiffness (Fig. 2). Additionally, microstructural evaluation revealed that the 0.10 mmol/L BAP sample experienced the greatest

reduction in pore size after 24 h of swelling, which likely contributed to reduced nutrient diffusion in the scaffold matrix. The combined effect of increased stiffness and reduced diffusion rates made GelMA with 0.10 mmol/L BAP unsuitable for culturing 3D encapsulated cells. These results are consistent with previous studies showing that while myoblasts in stiffer 3D environments tend to spread, proliferate, and enhance myogenesis compared to less dense matrices, extremely stiff environments activate apoptotic pathways [64]. In addition to 2D live/dead assays, phalloidin/DAPI staining of 3D encapsulated cultures further confirmed that cells remained viable and proliferated in the hydrogel matrices, providing complementary evidence of biocompatibility.

Although BAP induces time-dependent microstructural changes, swelling studies revealed that major differences in swelling ratio occurred only within the first few hours of immersion in PBS or culture media, after which the hydrogels stabilize (Figs. 4d–4f). This suggests that the overall structure stabilizes during the period of active cell adhesion and proliferation. Therefore, no significant long-term changes that might affect cell fate are expected during culture, which aligns with our observations of high viability and normal myogenic differentiation in BAP-containing hydrogels.

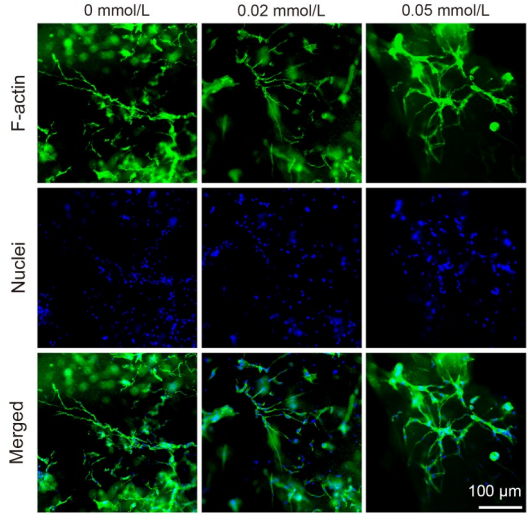

Fig. 8 Morphological analysis of C2C12 cells after 10 d of 3D encapsulation in 5% GelMA containing 0, 0.02, and 0.05 mmol/L BAP. Fluorescent images show C2C12 cell morphology throughout the culture period, with F-actin stained green using phalloidin and nuclei stained blue with DAPI, along with merged images

4 Conclusions

In this study, we developed and systematically evaluated a three-component BAP-based photoinitiator system for visible-light-induced photopolymerization of GelMA. Incorporating BAP considerably accelerated the photopolymerization process, with a considerable increase in rate as BAP concentration increased. In addition to faster crosslinking kinetics, BAP improved the mechanical properties of the resulting hydrogels, enhancing their structural stability for scaffold fabrication. Printing experiments showed that the BAP photoinitiator enabled the successful printing of low-concentration (5%) GelMA hydrogels under visible light. This allowed fabrication of well-defined structures and substantially reduced printing time, making the process as fast as or faster than conventional light-driven polymerization methods for GelMA. The addition of BAP to hydrogels causes internal structural changes during hydration after photocrosslinking, as shown by SEM imaging that reveals a more uniform distribution of smaller pores after 24 h of hydration. These structural reorganizations result in differences in swelling capacity across hydrogel samples. This unique behavior of BAP-containing hydrogels was used to create multilayer structures capable of dynamic deformation, demonstrating an example of 4D printing. Furthermore, cell viability assays confirmed that cells remained highly viable after exposure to the three-component photoinitiation system and, subsequently, within the resulting BAP-containing hydrogels, indicating biocompatibility. Cells embedded in BAP-containing hydrogels after 10 d showed elongated morphology, indicating successful adhesion, growth, and formation of cell chains, which suggests myogenesis. The addition of BAP improved the bioink properties, enabling high-resolution and rapid bioprinting. This improvement potentially halves the fabrication time while preserving biocompatibility and structural integrity.

Supplementary Information The online version contains supplementary material available at https://doi.org/10.1631/bdm.2500337.

Acknowledgements This work was supported by the Natural Sciences and Engineering Research Council of Canada (NSERC) Discovery Grant (No. RGPIN-2020-04559) and the Canada Foundation for Innovation John R. Evans Leaders Fund (JELF). The authors would like to thank Dr. Alan Aguirre-Soto (Tecnológico de Monterrey) for providing valuable advice regarding eosin Y behavior, Dr. Seonghwan Kim (University of Calgary) for providing access to the UV–Vis spectrometer, and Dr. Viki Kumar Prasad (University of Calgary) for discussions on the photoinitiation process.

Author contributions NTR: conceptualization, data curation, formal analysis, investigation, methodology, validation, visualization, writing—original draft, and writing—review & editing. KD: investigation, methodology, and writing—review & editing. AR: investigation, methodology, and writing—review & editing. KV: investigation, methodology, and writing—review & editing. GN: writing—review & editing. FM: writing—review & editing. HK: conceptualization, data curation, formal analysis, investigation, methodology, project administration, software, supervision, writing—original draft, and writing—review & editing. KK: conceptualization, project administration, resources, supervision, and writing—review & editing.

Declarations

Conflict of interest The authors declare that they have no conflict of interest.

Ethical approval This article does not contain any studies with human or animal subjects performed by any of the authors.

Data availability The data that support the findings of this study are available from the corresponding authors upon reasonable request.

Use of generative AI tools During the preparation of this work, the authors used ChatGPT in order to check for grammatical and typographical errors and improve language. After using this tool/service, the authors reviewed and edited the content as needed and take full responsibility for the content of the publication.

References

1. Lee TT, García JR, Paez JI et al (2015) Light-triggered in vivo activation of adhesive peptides regulates cell adhesion, inflammation and vascularization of biomaterials. *Nat Mater* 14(3):352–360. https://doi.org/10.1038/nmat4157
2. Rezaei NT, Dixit K, Kumar H et al (2023) Vascularized liver tissue embedded bioprinting utilizing GelMA/nanoclay-based composite hydrogels. bioRxiv. https://doi.org/10.1101/2023.11.16.567470
3. Rezaei NT, Kumar H, Liu HQ et al (2025) Bioprinting of hepatic tissue model using photocrosslinkable dECM-containing composite hydrogel. *Mater Today Bio* 32:101824. https://doi.org/10.1016/j.mtbio.2025.101824
4. Li J, Mo LT, Lu CH et al (2016) Functional nucleic acid-based hydrogels for bioanalytical and biomedical applications. *Chem Soc Rev* 45(5):1410–1431. https://doi.org/10.1039/c5cs00586h
5. Yuan M, Bi B, Huang JC et al (2018) Thermosensitive and photocrosslinkable hydroxypropyl chitin-based hydrogels for biomedical applications. *Carbohydr Polym* 192:10–18. https://doi.org/10.1016/j.carbpol.2018.03.031
6. Yue K, Trujillo-de Santiago G, Alvarez MM et al (2015) Synthesis, properties, and biomedical applications of gelatin methacryloyl (GelMA) hydrogels. *Biomaterials* 73:254–271. https://doi.org/10.1016/j.biomaterials.2015.08.045
7. Choi JR, Yong KW, Choi JY et al (2019) Recent advances in photo-crosslinkable hydrogels for biomedical applications. *Biotechniques* 66(1):40–53. https://doi.org/10.2144/btn-2018-0083
8. Kumar H, Sakthivel K, Mohamed MGA et al (2021) Designing gelatin methacryloyl (GelMA)-based bioinks for visible light stereolithographic 3D biofabrication. *Macromol Biosci* 21(1):2170001. https://doi.org/10.1002/mabi.202170001
9. Wang R, Yang ZG, Luo JR et al (2017) B_{12}-dependent photoresponsive protein hydrogels for controlled stem cell/protein release. *Proc Natl Acad Sci USA* 114(23):5912–5917. https://doi.org/10.1073/pnas.1621350114
10. Hossain Rakin R, Kumar H, Rajeev A et al (2021) Tunable metacrylated hyaluronic acid-based hybrid bioinks for stereolithography 3D bioprinting. *Biofabrication* 13(4):044109. https://doi.org/10.1088/1758-5090/ac25cb
11. Wang ZJ, Kumar H, Tian ZL et al (2018) Visible light photoinitiation of cell-adhesive gelatin methacryloyl hydrogels for stereolithography 3D bioprinting. *ACS Appl Mater Interfaces* 10(32): 26859–26869. https://doi.org/10.1021/acsami.8b06607
12. Kumar H, Ambhorkar P, Foulds I et al (2022) A kinetic model for predicting imperfections in bioink photopolymerization during visible-light stereolithography printing. *Addit Manuf* 55:102808. https://doi.org/10.1016/j.addma.2022.102808
13. Zennifer A, Manivannan S, Sethuraman S et al (2022) 3D bioprinting and photocrosslinking: emerging strategies & future perspectives. *Biomater Adv* 134:112576. https://doi.org/10.1016/j.msec.2021.112576
14. Allen NS (1996) Photoinitiators for UV and visible curing of coatings: mechanisms and properties. *J Photochem Photobiol A Chem* 100(1–3):101–107. https://doi.org/10.1016/S1010-6030(96)04426-7
15. Qin XH, Ovsianikov A, Stampfl J et al (2014) Additive manufacturing of photosensitive hydrogels for tissue engineering applications. *BioNanoMaterials* 15(3–4):49–70. https://doi.org/10.1515/bnm-2014-0008
16. Gauvin R, Chen YC, Lee JW et al (2012) Microfabrication of complex porous tissue engineering scaffolds using 3D projection stereolithography. *Biomaterials* 33(15):3824–3834. https://doi.org/10.1016/j.biomaterials.2012.01.048
17. Fairbanks BD, Schwartz MP, Bowman CN et al (2009) Photoinitiated polymerization of PEG-diacrylate with lithium phenyl-2,4,6-trimethylbenzoylphosphinate: polymerization rate and cytocompatibility. *Biomaterials* 30(35):6702–6707. https://doi.org/10.1016/j.biomaterials.2009.08.055
18. Ullrich G, Burtscher P, Salz U et al (2006) Phenylglycine derivatives as coinitiators for the radical photopolymerization of acidic aqueous formulations. *J Polym Sci A Polym Chem* 44(1):115–125. https://doi.org/10.1002/pola.21139
19. Shih H, Lin CC (2013) Visible-light-mediated thiol-ene hydrogelation using eosin-Y as the only photoinitiator. *Macromol Rapid Commun* 34(3):269–273. https://doi.org/10.1002/marc.201200605
20. Smith S, Maclean M, MacGregor SJ et al (2009) Exposure of 3T3 mouse fibroblasts and collagen to high intensity blue light. In*:* 13th International Conference on Biomedical Engineering, p.1352–1355. https://doi.org/10.1007/978-3-540-92841-6_333
21. Truong VX, Li FY, Ercole F et al (2018) Wavelength-selective coupling and decoupling of polymer chains via reversible [2 + 2] photocycloaddition of styrylpyrene for construction of cytocompatible photodynamic hydrogels. *ACS Macro Lett* 7(4):464–469. https://doi.org/10.1021/acsmacrolett.8b00099
22. Mironi-Harpaz I, Wang DY, Venkatraman S et al (2012) Photopolymerization of cell-encapsulating hydrogels: crosslinking efficiency versus cytotoxicity. *Acta Biomater* 8(5):1838–1848. https://doi.org/10.1016/j.actbio.2011.12.034
23. Lim KS, Klotz BJ, Lindberg GCJ et al (2019) Visible light cross-linking of gelatin hydrogels offers an enhanced cell microenvironment with improved light penetration depth. *Macromol Biosci* 19(6):e1900098. https://doi.org/10.1002/mabi.201900098
24. Noirbent G, Dumur F (2021) Photoinitiators of polymerization with reduced environmental impact: nature as an unlimited and renewable source of dyes. *Eur Polym J* 142:110109. https://doi.org/10.1016/j.eurpolymj.2020.110109
25. Wang ZJ, Abdulla R, Parker B et al (2015) A simple and high-resolution stereolithography-based 3D bioprinting system using visible light crosslinkable bioinks. *Biofabrication* 7(4):045009. https://doi.org/10.1088/1758-5090/7/4/045009
26. Greene T, Lin TY, Andrisani OM et al (2017) Comparative study of visible light polymerized gelatin hydrogels for 3D culture of hepatic progenitor cells. *J Appl Polym Sci* 134(11):44585. https://doi.org/10.1002/app.44585
27. Popielarz R, Vogt O (2008) Effect of coinitiator type on initiation

efficiency of two-component photoinitiator systems based on Eosin. *J Polym Sci A Polym Chem* 46(11):3519–3532. https://doi.org/10.1002/pola.22688
28. Sharifi S, Sharifi H, Akbari A et al (2021) Systematic optimization of visible light-induced crosslinking conditions of gelatin methacryloyl (GelMA). *Sci Rep* 11(1):23276. https://doi.org/10.1038/s41598-021-02830-x
29. Wang GN, Hill NS, Zhu D et al (2019) Efficient photoinitiating system based on diaminoanthraquinone for 3D printing of polymer/carbon nanotube nanocomposites under visible light. *ACS Appl Polym Mater* 1(5):1129–1135. https://doi.org/10.1021/acsapm.9b00140
30. Aguirre-Soto A, Kaastrup K, Kim S et al (2018) Excitation of metastable intermediates in organic photoredox catalysis: Z-scheme approach decreases catalyst inactivation. *ACS Catal* 8(7):6394–6400. https://doi.org/10.1021/acscatal.8b00857
31. Aguirre-Soto A, Hwang AT, Glugla D et al (2015) Coupled UV–Vis/FT–NIR spectroscopy for kinetic analysis of multiple reaction steps in polymerizations. *Macromolecules* 48(19):6781–6790. https://doi.org/10.1021/acs.macromol.5b01685
32. Noshadi I, Hong S, Sullivan KE et al (2017) *In vitro* and *in vivo* analysis of visible light crosslinkable gelatin methacryloyl (GelMA) hydrogels. *Biomater Sci* 5(10):2093–2105. https://doi.org/10.1039/c7bm00110j
33. Aguirre-Soto A, Kim S, Kaastrup K et al (2019) On the role of *N*-vinylpyrrolidone in the aqueous radical-initiated copolymerization with PEGDA mediated by eosin Y in the presence of O_2. *Polym Chem* 10(8):926–937. https://doi.org/10.1039/C8PY01459K
34. Zhang J, Lalevée J, Hill NS et al (2020) Substituent effects on photoinitiation ability of monoaminoanthraquinone-based photoinitiating systems for free radical photopolymerization under LEDs. *Macromol Rapid Commun* 41(18):e2000166. https://doi.org/10.1002/marc.202000166
35. Kumar H (2021) Light-Based Bioprinting for Fabricating Vascularized Tissues. PhD Thesis, University of British Columbia, Vancouver, Canada. https://doi.org/10.14288/1.0400478
36. Ma MH, Hao WW, Ma L et al (2018) Interception of radicals by molecular oxygen and diazo compounds: direct synthesis of oxalate esters using visible-light catalysis. *Org Lett* 20(18):5799–5802. https://doi.org/10.1021/acs.orglett.8b02487
37. Li JJ, Peng YY, Peña J et al (2021) An initiating system with high efficiency for PEGDA photopolymerization at 532 nm. *J Photochem Photobiol A Chem* 411:113216. https://doi.org/10.1016/j.jphotochem.2021.113216
38. Pynaert R, Buguet J, Croutxé-Barghorn C et al (2013) Effect of reactive oxygen species on the kinetics of free radical photopolymerization. *Polym Chem* 4(8):2475–2479. https://doi.org/10.1039/C3PY21163K
39. Lin JT, Liu HW, Chen KT et al (2019) Modeling the kinetics, curing depth, and efficacy of radical-mediated photopolymerization: the role of oxygen inhibition, viscosity, and dynamic light intensity. *Front Chem* 7:760. https://doi.org/10.3389/fchem.2019.00760
40. O'Brien AK, Bowman CN (2006) Modeling the effect of oxygen on photopolymerization kinetics. *Macromol Theory Simul* 15(2):176–182. https://doi.org/10.1002/mats.200500056
41. O'Brien AK, Bowman CN (2006) Impact of oxygen on photopolymerization kinetics and polymer structure. *Macromolecules* 39(7):2501–2506. https://doi.org/10.1021/ma051863l
42. Wang S, Li L, Su D et al (2018) Patterning porosity in hydrogels by arresting phase separation. *ACS Appl Mater Interfaces* 10(40):34604–34610. https://doi.org/10.1021/acsami.8b11530
43. Müller MZ, Style RW, Müller R et al (2022) A phase-separating thiol-ene photoresin for volumetric bioprinting of macroporous hydrogels. bioRxiv. https://doi.org/10.1101/2022.01.29.478338
44. Liu B, Li H, Meng FZ et al (2024) 4D printed hydrogel scaffold with swelling-stiffening properties and programmable deformation for minimally invasive implantation. *Nat Commun* 15(1):1587. https://doi.org/10.1038/s41467-024-45938-0
45. Feng WJ, Wang ZK (2023) Tailoring the swelling-shrinkable behavior of hydrogels for biomedical applications. *Adv Sci* 10(28):e2303326. https://doi.org/10.1002/advs.202303326
46. Blacklow SO, Li J, Freedman BR et al (2019) Bioinspired mechanically active adhesive dressings to accelerate wound closure. *Sci Adv* 5(7):eaaw3963. https://doi.org/10.1126/sciadv.aaw3963
47. Liao J, Huang HH (2020) Smart pH/magnetic sensitive *Hericium erinaceus* residue carboxymethyl chitin/Fe_3O_4 nanocomposite hydrogels with adjustable characteristics. *Carbohydr Polym* 246:116644. https://doi.org/10.1016/j.carbpol.2020.116644
48. Fang W, Yang L, Hong LJ et al (2021) A chitosan hydrogel sealant with self-contractile characteristic: from rapid and long-term hemorrhage control to wound closure and repair. *Carbohydr Polym* 271:118428. https://doi.org/10.1016/j.carbpol.2021.118428
49. Gangrade A, Gawali B, Jadi PK et al (2020) Photo-electro active nanocomposite silk hydrogel for spatiotemporal controlled release of chemotherapeutics: an in vivo approach toward suppressing solid tumor growth. *ACS Appl Mater Interfaces* 12(25):27905–27916. https://doi.org/10.1021/acsami.0c02470
50. Gong JX, Schuurmans CCL, van Genderen AM et al (2020) Complexation-induced resolution enhancement of 3D-printed hydrogel constructs. *Nat Commun* 11:1267. https://doi.org/10.1038/s41467-020-14997-4
51. Zhao H, Huang YM, Lv FT et al (2021) Biomimetic 4D-printed breathing hydrogel actuators by nanothylakoid and thermoresponsive polymer networks. *Adv Funct Mater* 31(49):2105544. https://doi.org/10.1002/adfm.202105544
52. Zhao XH, Huebsch N, Mooney DJ et al (2010) Stress-relaxation behavior in gels with ionic and covalent crosslinks. *J Appl Phys* 107(6):063509. https://doi.org/10.1063/1.3343265
53. Wang YP, Chen YZ, Zheng JN et al (2022) Three-dimensional printing self-healing dynamic/photocrosslinking gelatin-hyaluronic acid double-network hydrogel for tissue engineering. *ACS Omega* 7(14):12076–12088. https://doi.org/10.1021/acsomega.2c00335
54. Yoon HJ, Shin SR, Cha JM et al (2016) Cold water fish gelatin methacryloyl hydrogel for tissue engineering application. *PLoS ONE* 11(10):e0163902. https://doi.org/10.1371/journal.pone.0163902
55. Ligon SC, Husár B, Wutzel H et al (2014) Strategies to reduce oxygen inhibition in photoinduced polymerization. *Chem Rev* 114(1):557–589. https://doi.org/10.1021/cr3005197

56. Tozar T, Nistorescu S, Boni M et al (2022) Pulsed laser photocrosslinking of gelatin methacryloyl hydrogels for the controlled delivery of chlorpromazine to combat antimicrobial resistance. *Pharmaceutics* 14(10):2121. https://doi.org/10.3390/pharmaceutics14102121
57. Mulakkal MC, Trask RS, Ting VP et al (2018) Responsive cellulose-hydrogel composite ink for 4D printing. *Mater Des* 160: 108–118. https://doi.org/10.1016/j.matdes.2018.09.009
58. Zhao ZA, Kuang X, Yuan C et al (2018) Hydrophilic/Hydrophobic composite shape-shifting structures. *ACS Appl Mater Interfaces* 10(23):19932–19939. https://doi.org/10.1021/acsami.8b02444
59. Champeau M, Heinze DA, Viana TN et al (2020) 4D printing of hydrogels: a review. *Adv Funct Mater* 30(31):1910606. https://doi.org/10.1002/adfm.201910606
60. Zhao ZA, Wu JT, Mu XM et al (2017) Desolvation induced origami of photocurable polymers by digit light processing. *Macromol Rapid Commun* 38(13):1600625. https://doi.org/10.1002/marc.201600625
61. Dong YT, Wang SC, Ke YJ et al (2020) 4D printed hydrogels: fabrication, materials, and applications. *Adv Mater Technol* 5(6): 2000034. https://doi.org/10.1002/admt.202000034
62. Zhao X, Lang Q, Yildirimer L et al (2016) Photocrosslinkable gelatin hydrogel for epidermal tissue engineering. *Adv Healthc Mater* 5(1):108–118. https://doi.org/10.1002/adhm.201500005
63. Chen CS, Mrksich M, Huang S et al (1997) Geometric control of cell life and death. *Science* 276(5317):1425–1428. https://doi.org/10.1126/science.276.5317.1425
64. Costantini M, Testa S, Fornetti E et al (2017) Engineering muscle networks in 3D gelatin methacryloyl hydrogels: influence of mechanical stiffness and geometrical confinement. *Front Bioeng Biotechnol* 5:22. https://doi.org/10.3389/fbioe.2017.00022